# Sensitivity Enhancement and Random Telegraph Noise in Magnetic Tunnel Junctions with Compensated Anisotropy

Guanyang He, Yiou Zhang, and Gang Xiao

Phys. Rev. Applied **19**, 024069 — Published 27 February 2023

DOI: 10.1103/PhysRevApplied.19.024069

# Sensitivity Enhancement and Random Telegraph Noise in Magnetic Tunnel Junctions with Compensated Anisotropy

*Guanyang He, Yiou Zhang, and Gang Xiao*[*]

Department of Physics, Brown University, Providence, RI 02912, USA

## ABSTRACT

We demonstrated the manipulation of perpendicular magnetic anisotropy (PMA) in magnetic tunnel junctions (MTJs) by varying the layer stacks and temperature. PMA is tuned to compensate with the shape anisotropy, giving a non-hysteretic magnetic response, a noteworthy sensitivity enhancement, and a field detectability of 1.8 nT/$\sqrt{Hz}$ at 100 kHz. Such a method is further exemplified in multiple MTJs, providing a solution to obtain desired sensitivities and operating temperatures. Additionally, the electronic noise of this MTJ is revealed as a random telegraph noise (RTN) due to a generation-recombination process. The observed voltage-dependent RTN could potentially be applied to true random number generators.

*Email: Gang_Xiao@brown.edu

## I. INTRODUCTION

Magnetic tunnel junction (MTJ) is a magnetoresistance device extensively applied in magnetic field sensing or biomedical imaging, with its advantages include large signals, low power consumption, and CMOS compatibility.[1, 2] For magnetic sensors based on MTJs, the elimination of hysteresis has always been critical, where solutions related to the hard-axis bias field, shape anisotropy, superparamagnetism, and interfacial perpendicular magnetic anisotropy (PMA) have all been explored.[3-6] While most linearization strategies come at the cost of sensitivity, specific hard-axis bias fields could actually enhance the sensitivity[7, 8]. Since PMA with its easy tunability[9, 10] can also act as an effective field in the out-of-plane direction, similar enhancement may be expected. Focusing on this idea, we have already shown that the compensation of magnetic anisotropy leads to excellent sensing performances in sensors based on anomalous Hall effect (AHE).[11, 12] In this work, we demonstrate that introduction of PMA in MTJ sensors not only eliminates the hysteresis but also boosts the sensitivity. By optimizing the PMA strength using varying layer thicknesses and annealing treatments, we characterize the magnetic sensing performances of this class of MTJs in a broad temperature range from 140 K to 400 K.

## II. EXPERIMENTAL

Following relevant literature, [13-15] we have used a modified layer structure in our MTJs which effectively induces PMA in its synthetic free layer; it is sequenced as: $Si/SiO_2$/Ta(50)/Ru(150)/Ta(100)/MgO(16)/FL/MgO(27)/$Co_{40}Fe_{40}B_{20}$(30)/Ru(8.5)/$Co_{50}Fe_{50}$(30)/ $Ir_{22}Mn_{78}$(180)/Ru(100)/Ta(100). The numbers in parentheses represent the thickness of each layer in angstrom. The free-layer (FL) consists of $Co_{40}Fe_{40}B_{20}$(9)/W($t_W$)/$Co_{40}Fe_{40}B_{20}$($t_{CFB}$) where the two CoFeB layers are coupled by Ruderman–Kittel–Kasuya–Yosida (RKKY) interaction through the W spacer. We used magnetron sputtering to deposit the complete MTJ with a base pressure of $2\times10^{-8}$ torr. Photolithography and physical ion milling were used to define MTJ elements into an oval shape of a lateral size $7 \times 10.5\ \mu m^2$. After fabrication, thermal annealing was performed at temperature $T_a$ for one hour in high vacuum, under a magnetic field of 0.45 T along the long-axis direction of the MTJ oval. In all our magneto-transport measurements conducted in the Quantum Design® Physical Property Measurement System (PPMS), eight identical MTJs were connected in series as a sensor unit, exposed to in-plane magnetic fields applied in the long-axis direction

(magnetic easy-axis) of each MTJ oval by. The resistance-area product of MTJs is typically 60 $k\Omega\ \mu m^2$, giving a total resistance of 8 $k\Omega$ for 8 MTJ elements in series. Thus, the contact resistance (around 1 Ω) is negligible in our two-probe electrical measurements. The MTJ sensor was powered by batteries and connected in series with a voltage divider resistor during measurements. The bias voltage across the MTJ sensor was 0.3 V, or 37.5 mV per MTJ element. The field sensitivity was experimentally determined by its voltage response to a modulating field ($\delta H = 0.3\ Oe$) at 5 Hz. In literature, the sensitivity is roughly related to the magnetic anisotropy through the transfer curve.[16, 17] Unless the sensor is hysteresis-free, the sensitivity overestimated this way could deviate from the real values in low-field measurements.[18]

## III. RESULTS AND DISCUSSION

Fig. 1 shows the TMR transfer curves of MTJs at 300 K with various layer thickness and annealing temperature ($T_a$). In Fig. 1(a), while fixing the CoFeB thickness $t_{CFB} = 14.3$ Å and $T_a = 300$ ℃ , we vary the W spacer thickness $t_W$ from 8 Å to 4 Å. The coercivity collapses and the saturation field increases, implying that PMA strength is weaker for thicker spacer. This is because in the composite free-layer $Co_{40}Fe_{40}B_{20}(9)/W(t_W)/Co_{40}Fe_{40}B_{20}(t_{CFB})$, two CoFeB layers are coupled by RKKY interaction. Both sides of the FL is neighbored with MgO for the interfacial PMA.[14] In the first 9 Å thin CoFeB layer the magnetic moments are mostly in the out-of-plane direction; the moments in the second CoFeB layer tend to be aligned the same way due to their magnetic coupling. Such coupling serves as an additional source of PMA effectively. Therefore, if the increment in spacer thickness $t_W$ impairs this coupling, the PMA in the second CoFeB layer would become weaker. This is likely because the RKKY strength is reported to have non-monotonic or oscillatory relations with the spacer layer thickness.[19-21] Similar trend can be observed when $t_{CFB}$ is varied with $t_W = 6$ Å, $T_a = 300$ ℃ fixed, as shown in Fig. 1(b). This is a straightforward result of PMA decreasing with the film thickness. Finally, as shown in Fig. 1(c), PMA strength is also enhanced as $T_a$ increases from 280 ℃ to 300 ℃, for $t_W = 6$ Å and $t_{CFB} = 13.5$ Å. Combining these results, stronger PMA is present in MTJs with thinner CoFeB layer and W spacer, as well as higher $T_a$. The PMA in the free layer of MTJ reduces and eventually eliminates the magnetic hysteresis, which also leads to large saturation fields and low TMR ratios.

Fig. 2(a) shows the TMR transfer curves from 140 K to 400 K in MTJs with $t_W = 6$ Å, while $t_{CFB} = 13.9$ Å and $T_a = 300$ ℃ are fixed. While the saturation field increases monotonically as temperature decreases, the coercivity increases after reaching a minimum at 340 K, as shown in Fig. 2(b). As a crucial factor influencing the transfer curves, the PMA strength in MTJs is known to be tunable by temperature.[22] However, the uncommon temperature dependence of the transfer curves here cannot be explained solely by a temperature-dependent PMA, which should be derived from regions with different PMA strengths in the MTJ free layer. This inhomogeneity of PMA could originate from a thickness variation or boundary effect. To simplify the scenario, we assume the existence of "P-regions" with strong PMA, and "I-regions" with weak PMA (more in-plane magnetization). Nevertheless, a direct observation of these two regions by magneto-opto-Kerr-effect (MOKE) microscope or magnetic-force-microscope (MFM) is difficult, because a thick protective capping layer is used to preserve the interface of CoFeB/W or CoFeB/MgO where PMA originates. Such capping layer suppresses optical signals from CoFeB for MOKE and elongates the lift-off distance for the MFM tip. Therefore, using thinner capping layers in this MTJ device would be appealing in future studies, or measuring it by X-ray photoemission electron microscopy (X-PEEM).

To manifest the behavior of a MTJ free layer with P-regions and I-regions, micromagnetic simulations are performed by Mumax software. At each temperature and external field, the simulation runs for 5 ns to account for the dynamic effect at finite temperature. In the simulation the exchange stiffness of the CoFeB free layer is appropriately set as 15 pJ/m, and the saturation magnetization is temperature ($T$) dependent as $M_0[1-(T/T_C)^{1.5}]$,[23] with $M_0 = 1.46 \times 10^6$ A/m, $T_C = 1120$ K.[24] The Landau-Lifshitz damping coefficient is 0.1. The shape of free layer is set to be an oval with a major axis of 10.5 $\mu m$, a minor axis of 7 $\mu m$, and a thickness of 13.9 Å; every setting stays the same as the sample of Fig. 2(a). The temperature dependent PMA takes the form of $K_0[1-(T/T_C)^{1.5}]^3$;[23] for P-region, $K_0 = 15.5 \times 10^5$ J/m$^3$ matches well with experiments, and for I-region $K_0 = 13.8 \times 10^5$ J/m$^3$. Regions of different PMA are considered to be weakly exchange-coupled across grain boundaries as in the literature[25], with 50% exchange coupling strength. Two kinds of regions are randomly distributed in the MTJ oval, with a configuration shown in Fig. 2(c); P-regions with stronger PMA are exhibited with brighter colors. The magnetization transfer curves of P-region, I-region and the total free layer are shown in Fig. 2(d), 2(e), 2(f), respectively. At high temperatures above 300 K, PMA is so negligible that two regions

show similar transfer curves. As temperature drops to around 200 K, the saturation field in Fig. 2(f) increases due to the enhanced PMA in P-regions. The magnetic moments in P-regions can hardly be aligned with the in-plane magnetic fields because of the strong PMA, as in Fig. 2(d) the saturation field rises beyond the field range of simulation. The increased saturation field is also accompanied by smaller permeabilities in both Fig. 2(d) and (f). Meanwhile, the coercivity is enlarged with decreasing temperature in Fig. 2(f), which is mostly contributed by the hysteretic I-regions as in Fig. 2(e). With dominant in-plane shape anisotropies and multi-domain features, clear coercivity exists in I-regions and increases at lower temperatures due to the thermal-assisted domain nucleation and propagation[26]. Therefore, the characteristics of simulated Fig. 2(f) are understood and correspond well with the experimental results in Fig. 2(a) qualitatively. What is missing is the minimum of coercivity in Fig. 2(a) with no correspondence in Fig. 2(f). Such vanishing coercivity only appears at the spin-reorientation from out-of-plane to in-plane direction in the free layer, where PMA is just enough to compensate the in-plane anisotropy. Such a critical compensation is difficult to find in simulations, but we will illustrate it more with experimental results in the next paragraph. In addition, simulations for another configuration of P-regions and I-regions are shown in Fig. 3 of the Supplementary, where two regions are more well-defined instead of randomly distributed. The increment of coercivity due to domain nucleation and propagation at low temperatures is not matched in Fig. 3, implying that the random distribution of two regions is closer to the experiments.

Generally speaking, magnetic moments in I-regions are more responsive to the external in-plane fields, contributing more sensitivity and noise, and the moments in the P-region make the overall performance less coercive. The sensitivity map of this MTJ under different temperatures and magnetic fields is given in Fig. 4(a). It is noteworthy that the maximum sensitivity is reached at 370 K, where coercivity is the smallest, yet the slope of DC transfer curve is not the largest in Fig. 2(a). It corresponds to the spin-reorientation in the free layer, where magnetic moments can rotate freely and contribute very large sensitivity. This reveals an important fact that the actual sensitivity to small magnetic fields cannot be solely estimated from the transfer curve slope. Even tiny coercivity can lock the magnetic moments in low-field measurements, regardless of the overall transfer curve. The noise spectral density is obtained and normalized by the bias voltage on the sensor, and its value at 1 Hz and 100 kHz are respectively shown in Fig. 4(b) and (d). At both frequencies, the noise level is high in the sensing region and low at large fields (magnetically

saturated), which implies it is mostly contributed by magnetic fluctuation[27]. In Fig. 4(c) and (e), the sensor detectability at 1Hz and 100 kHz is calculated by the ratio between the noise and the sensitivity. In Table I, our result is compared with MTJs adopting other linearization strategies, and AHE sensors. Our MTJ sensors with compensated magnetic anisotropy have exhibited higher sensitivity than most of them. MTJs with a soft pinned free layer also show high sensitivity, yet their magnetic field detectability is worse than ours. Therefore, our sensor turns out a good candidate combining high sensitivity and good field detectability. Nevertheless, the scaling relation between low-frequency noise and sensitivity, as shown in Fig. 4(f), is quadratic. For sensors with quadratic scaling relation, higher sensitivity won't provide better low-frequency detectability.[5, 11, 24]

We further measured the sensitivities of four MTJs with multiple $t_{CFB}$ and $T_a$ values, while $t_W = 6$ Å fixed. For a fair comparison, the maximum sensitivity $S_P$ in $\pm 50\ Oe$ field range at each measurement temperature is recorded, since the offset field changes under different $T_a$ in Fig. 1(c). As shown in Fig. 5(a), $S_P$ for all samples first increases then decreases with the measurement temperature, yet the peak positions are different. Further, we determined the in-plane saturation field $H_S$ from the area between the hysteresis loop and the magnetic field axis [22, 24], as an effective indicator of the PMA strength. In Fig. 5(b), while $H_S$ varies for various samples under different measurement temperatures, the peak of $S_P$ always falls in the same region of $H_S$. With such a clear correlation between $S_P$ and $H_S$, the desired sensitivity and operating temperature of an MTJ sensor can be reached by tuning $H_S$, through the layer thickness and annealing conditions.

On the other hand, in this MTJ with interfacial PMA, random telegraph noise (RTN) exists with a Lorentzian spectrum, under a saturation field of 400 Oe where magnetic noise is suppressed. Experimentally, we measured a single MTJ with the same layer structure of the one in Fig. 4, in a circular shape of 5 μm diameter. The temperature-dependent noise spectrum is shown in Fig. 6(a). At 150 K, the noise conforms to a typical 1/f relation. At 300 K, a bump appears due to the RTN noise, with a roll-off frequency near 10 Hz. As temperature rises to 380 K, the roll-off frequency gradually shifts to higher frequencies of a few hundred Hz, and the bump amplitude drops. Corresponding time-domain signals are shown in the inset. At 300 K, the two-level flipping is evident, with a long relaxation time near 0.1 s in one state; at 380 K, the flipping becomes more rapid with a 1 ms relaxation time.

RTN in MTJs has usually been contributed by magnetic quasi-stable domain states in the free layer[28], but here we attribute RTN to an electrical generation-recombination (GR) process, as the MTJ is magnetically saturated. First, the energy of electrons in the conductive state of MTJ can be altered by eV due to the bias voltage V.[29, 30] During the tunneling process across the barrier, the conducting electrons may be trapped by localized states either inside the MgO barrier[31, 32] or at CoFeB/MgO interface[32], with a corresponding energy barrier preventing the flipping between the trapped state and the conductive state. Electrons get trapped by chance and return to the conductive state after a relaxation time. Such GR process leads to a fluctuation in the charge carrier density and corresponding two-level voltage signals, which can be described as:[33]

$$\begin{cases} \tau_t = \tau_0 \exp\left(\frac{\Delta E_1}{\gamma k_B \mathrm{T}}\right) \\ \tau_c = \tau_0 \exp\left(\frac{\Delta E_2 + eV}{\gamma k_B \mathrm{T}}\right) \\ V = a + bT \end{cases} \Rightarrow \begin{cases} \ln(\tau_t) = \frac{E_0}{\gamma k_B}(\frac{1}{T}) + \ln(\tau_0) \\ \ln(\tau_c) = \frac{E_0 + ea}{\gamma k_B}(\frac{1}{T}) + \frac{b}{\gamma k_B} + \ln(\tau_0) \end{cases} \quad (1)$$

$\tau_t, \tau_c$ are the relaxation time of the trapping state and conductive state respectively, where electrons spend much less time being locally trapped. T is the temperature, $\tau_0$ an attempt time in the nanosecond range for an electron migration process, and $\gamma$ an empirical constant. In our experimental setup, the bias voltage changes when the tunneling resistance of MTJ decreases with rising temperature,[2] with a temperature coefficient much larger than the serial resistor. The relation between bias voltage and temperature is thus calibrated to be $V = a + bT, a = 0.3\,V, b = -1.87 \times 10^{-4}\,V/K$. Such small voltage change should have negligible effect on overall sensing properties.[34] $\Delta E_1$ is the energy barrier the trapped electron needs to overcome before flipping into the conductive state, and it is $\Delta E_2 + eV$ for the conductive state vice versa. To verify this model, we have collected the average relaxation time $\tau_t, \tau_c$ in 30 seconds at various temperatures. The results are plotted in Fig. 6(b) in a semi-log scale where an expected linear relation is found between $\ln(\tau_t), \ln(\tau_c)$ and $1/\mathrm{T}$. If we further assume that $\Delta E_2 \approx \Delta E_1$, the fitting indicates $\Delta E_1 = \Delta E_2 = 2.59 \times 10^{-19} J$ and $\gamma = 2.84$. In addition, multiple Lorentzian spectra in Fig. 6(a) can be reconstructed by general RTN theory:

$$S(f) = \frac{4(\Delta V)^2}{(\tau_t + \tau_c)[(1/\tau_t + 1/\tau_c)^2 + (2\pi f)^2]} \quad (2)$$

where $\Delta V$ is the voltage difference between two flipping states in the inset of Fig. 6(a).

## IV. CONCLUSION

We have revealed the PMA strength in an MTJ free layer versus its spacer layer thickness, free layer thickness, and annealing temperature, which provides levers to manipulate the magnetic anisotropy in the free layer. The inhomogeneity of PMA, the competition between PMA and shape anisotropy and its correlation with sensing performances are discussed in detail. In multiple MTJ sensors with different fabrication conditions, we have illustrated that the compensation of magnetic anisotropy can be used as a means to increase the field detectability to 1.8 nT/$\sqrt{Hz}$ at 100 kHz, and to modify the operating temperature of an MTJ device. Moreover, RTN is observed and explained by an electrical generation-recombination process in this device. Such a voltage-dependent RTN could potentially be utilized in true random number generators, similarly to the utilization of thermal noise in superparamagnetic MTJs.[35]


## ACKNOWLEDGMENTS

The work was supported by the National Science Foundation (NSF) under Grant No. OMA-1936221. Y.Z. acknowledges support from Fermilab-Graduate Instrumentation Research Award from DOE grant number DE-AC05-00OR22725. We used the Heidelberg MLA150 Maskless Aligner supported by National Science Foundation Grant No. DMR-1827453.

## Refernces:


1. B. Dieny, I. L. Prejbeanu, K. Garello, P. Gambardella, P. Freitas, R. Lehndorff, W. Raberg, U. Ebels, S. O. Demokritov, and J. Akerman, Opportunities and challenges for spintronics in the microelectronics industry. *Nature Electronics* 3(8):446-459 (2020).
2. G. Xiao Magnetoresistive sensors based on magnetic tunneling junctions. *Handbook of Spin Transport and Magnetism*, eds Tsymbal EY & Zutic I (CRC press, Taylor & Francis, Boca Raton, FL, USA) (2012).
3. X. Liu, C. Ren, and G. Xiao, Magnetic tunnel junction field sensors with hard-axis bias field. *Journal of Applied Physics* 92(8):4722-4725 (2002).
4. Y. Lu, R. Altman, A. Marley, S. Rishton, P. Trouilloud, G. Xiao, W. Gallagher, and S. Parkin, Shape-anisotropy-controlled magnetoresistive response in magnetic tunnel junctions. *Applied physics letters* 70(19):2610-2612 (1997).
5. Y. Zhang, G. He, X. Zhang, and G. Xiao, Magnetotransport and electronic noise in superparamagnetic magnetic tunnel junctions. *Applied Physics Letters* 115(2):022402 (2019).
6. Z. Zeng, P. Khalili Amiri, J. Katine, J. Langer, K. Wang, and H. Jiang, Nanoscale magnetic tunnel junction sensors with perpendicular anisotropy sensing layer. *Applied Physics Letters* 101(6):062412 (2012).
7. W. Zhang, G. Xiao, and M. J. Carter, Two-dimensional field-sensing map and magnetic anisotropy dispersion in magnetic tunnel junction arrays. *Physical Review B* 83(14):144416 (2011).
8. D. Mazumdar, W. Shen, X. Liu, B. Schrag, M. Carter, and G. Xiao, Field sensing characteristics of magnetic tunnel junctions with (001) MgO tunnel barrier. *Journal of applied physics* 103(11):113911 (2008).
9. D.-T. Quach, Q.-H. Tran, K. Møhave, and D.-H. Kim, Perpendicular magnetic anisotropy and the magnetization process in CoFeB/Pd multilayer films. *Journal of Physics D: Applied Physics* 47(44):445001 (2014).
10. O. Bultynck, M. Manfrini, A. Vaysset, J. Swerts, C. J. Wilson, B. Sorée, M. Heyns, D. Mocuta, I. P. Radu, and T. Devolder, Instant-on spin torque in noncollinear magnetic tunnel junctions. *Physical Review Applied* 10(5):054028 (2018).
11. Y. Zhang, K. Wang, and G. Xiao, Noise characterization of ultrasensitive anomalous Hall effect sensors based on Co40Fe40B20 thin films with compensated in-plane and perpendicular magnetic anisotropies. *Applied Physics Letters* 116(21):212404 (2020).
12. K. Wang, Y. Zhang, and G. Xiao, Anomalous Hall Sensors with High Sensitivity and Stability Based on Interlayer Exchange-Coupled Magnetic Thin Films. *Physical Review Applied* 13(6):064009 (2020).
13. M. Wang, Y. Zhang, X. Zhao, and W. Zhao, Tunnel junction with perpendicular magnetic anisotropy: Status and challenges. *Micromachines* 6(8):1023-1045 (2015).
14. W. Skowroński, M. Czapkiewicz, S. Ziętek, J. Chęciński, M. Frankowski, P. Rzeszut, and J. Wrona, Understanding stability diagram of perpendicular magnetic tunnel junctions. *Scientific reports* 7(1):1-6 (2017).
15. M. Wang, W. Cai, K. Cao, J. Zhou, J. Wrona, S. Peng, H. Yang, J. Wei, W. Kang, and Y. Zhang, Current-induced magnetization switching in atom-thick tungsten engineered perpendicular magnetic tunnel junctions with large tunnel magnetoresistance. *Nature communications* 9(1):1-7 (2018).

16. T. Nakano, M. Oogane, H. Naganuma, and Y. Ando, Systematic investigation on correlation between sensitivity and nonlinearity in magnetic tunnel junction for magnetic sensor. *IEEE Transactions on Magnetics* 51(11):1-4 (2015).
17. P. Wisniowski, J. Wrona, T. Stobiecki, S. Cardoso, and P. Freitas, Magnetic tunnel junctions based on out-of-plane anisotropy free and in-plane pinned layer structures for magnetic field sensors. *IEEE transactions on magnetics* 48(11):3840-3842 (2012).
18. G. He, Y. Zhang, L. Qian, G. Xiao, Q. Zhang, J. C. Santamarina, T. W. Patzek, and X. Zhang, PicoTesla magnetic tunneling junction sensors integrated with double staged magnetic flux concentrators. *Applied Physics Letters* 113(24):242401 (2018).
19. J. Chatterjee, S. Auffret, R. Sousa, P. Coelho, I.-L. Prejbeanu, and B. Dieny, Novel multifunctional RKKY coupling layer for ultrathin perpendicular synthetic antiferromagnet. *Scientific reports* 8(1):1-9 (2018).
20. J. Chen, S. Peng, D. Xiong, H. Cheng, H. Zhou, Y. Jiang, J. Lu, W. Li, and W. Zhao, Correlation of interfacial perpendicular magnetic anisotropy and interlayer exchange coupling in CoFe/W/CoFe structures. *Journal of Physics D: Applied Physics* (2020).
21. S. S. Parkin, Systematic variation of the strength and oscillation period of indirect magnetic exchange coupling through the 3d, 4d, and 5d transition metals. *Physical Review Letters* 67(25):3598 (1991).
22. J. G. Alzate, P. Khalili Amiri, G. Yu, P. Upadhyaya, J. A. Katine, J. Langer, B. Ocker, I. N. Krivorotov, and K. L. Wang, Temperature dependence of the voltage-controlled perpendicular anisotropy in nanoscale MgO| CoFeB| Ta magnetic tunnel junctions. *Applied physics letters* 104(11):112410 (2014).
23. K.-M. Lee, J. W. Choi, J. Sok, and B.-C. Min, Temperature dependence of the interfacial magnetic anisotropy in W/CoFeB/MgO. *AIP Advances* 7(6):065107 (2017).
24. G. He, Y. Zhang, and G. Xiao, Nonhysteretic Vortex Magnetic Tunnel Junction Sensor with High Dynamic Reserve. *Physical Review Applied* 14(3):034051 (2020).
25. H. Sepehri-Amin, T. Ohkubo, M. Gruber, T. Schrefl, and K. Hono, Micromagnetic simulations on the grain size dependence of coercivity in anisotropic Nd–Fe–B sintered magnets. *Scripta Materialia* 89:29-32 (2014).
26. H. Liu, R. Wang, P. Guo, Z. Wen, J. Feng, H. Wei, X. Han, Y. Ji, and S. Zhang, Manipulation of magnetization switching and tunnel magnetoresistance via temperature and voltage control. *Scientific reports* 5:18269 (2015).
27. Z. Lei, G. Li, W. F. Egelhoff, P. Lai, and P. W. Pong, Review of noise sources in magnetic tunnel junction sensors. *IEEE Transactions on Magnetics* 47(3):602-612 (2011).
28. T. Arakawa, T. Tanaka, K. Chida, S. Matsuo, Y. Nishihara, D. Chiba, K. Kobayashi, T. Ono, A. Fukushima, and S. Yuasa, Low-frequency and shot noises in CoFeB/MgO/CoFeB magnetic tunneling junctions. *Physical Review B* 86(22):224423 (2012).
29. Y. Sakuraba, K. Takanashi, Y. Kota, T. Kubota, M. Oogane, A. Sakuma, and Y. Ando, Evidence of Fermi level control in a half-metallic Heusler compound Co 2 MnSi by Al-doping: Comparison of measurements with first-principles calculations. *Physical Review B* 81(14):144422 (2010).
30. Y. Lu, X. Li, G. Xiao, R. Altman, W. Gallagher, A. Marley, K. Roche, and S. Parkin, Bias voltage and temperature dependence of magnetotunneling effect. *Journal of applied physics* 83(11):6515-6517 (1998).

31. J. Teixeira, J. Ventura, J. Araujo, J. Sousa, P. Wisniowski, S. Cardoso, and P. Freitas, Resonant tunneling through electronic trapping states in thin MgO magnetic junctions. *Physical review letters* 106(19):196601 (2011).
32. Z. Diao, J. F. Feng, H. Kurt, G. Feng, and J. M. D. Coey, Reduced low frequency noise in electron beam evaporated MgO magnetic tunnel junctions. *Applied Physics Letters* 96(20):202506 (2010).
33. C. Rogers and R. Buhrman, Composition of 1 f Noise in Metal-Insulator-Metal Tunnel Junctions. *Physical review letters* 53(13):1272 (1984).
34. W. Skowroński, P. Wiśniowski, T. Stobiecki, S. Cardoso, P. P. Freitas, and S. van Dijken, Magnetic field sensor with voltage-tunable sensing properties. *Applied Physics Letters* 101(19):192401 (2012).
35. D. Vodenicarevic, N. Locatelli, A. Mizrahi, J. S. Friedman, A. F. Vincent, M. Romera, A. Fukushima, K. Yakushiji, H. Kubota, and S. Yuasa, Low-energy truly random number generation with superparamagnetic tunnel junctions for unconventional computing. *Physical Review Applied* 8(5):054045 (2017).
36. W. Z. Zhang, Q. Hao, and G. Xiao, Low-frequency noise in serial arrays of MgO-based magnetic tunnel junctions. *Physical Review B* 84(9):094446 (2011).
37. Y. Zhang, G. Y. He, X. X. Zhang, and G. Xiao, Magnetotransport and electronic noise in superparamagnetic magnetic tunnel junctions. *Applied Physics Letters* 115(2):022402 (2019).
38. J. P. Valadeiro, J. Amaral, D. C. Leitao, R. Ferreira, S. F. Cardoso, and P. J. P. Freitas, Strategies for pTesla Field Detection Using Magnetoresistive Sensors With a Soft Pinned Sensing Layer. *Ieee Transactions on Magnetics* 51(1):1-4 (2015).
39. S.-H. Liou, D. Sellmyer, S. E. Russek, R. Heindl, F. Da Silva, J. Moreland, D. P. Pappas, L. Yuan, and J. Shen. Magnetic noise in a low-power picotesla magnetoresistive sensor. *SENSORS, 2009 IEEE*, (IEEE), pp 1848-1851 (2009).

## Figures and Captains:

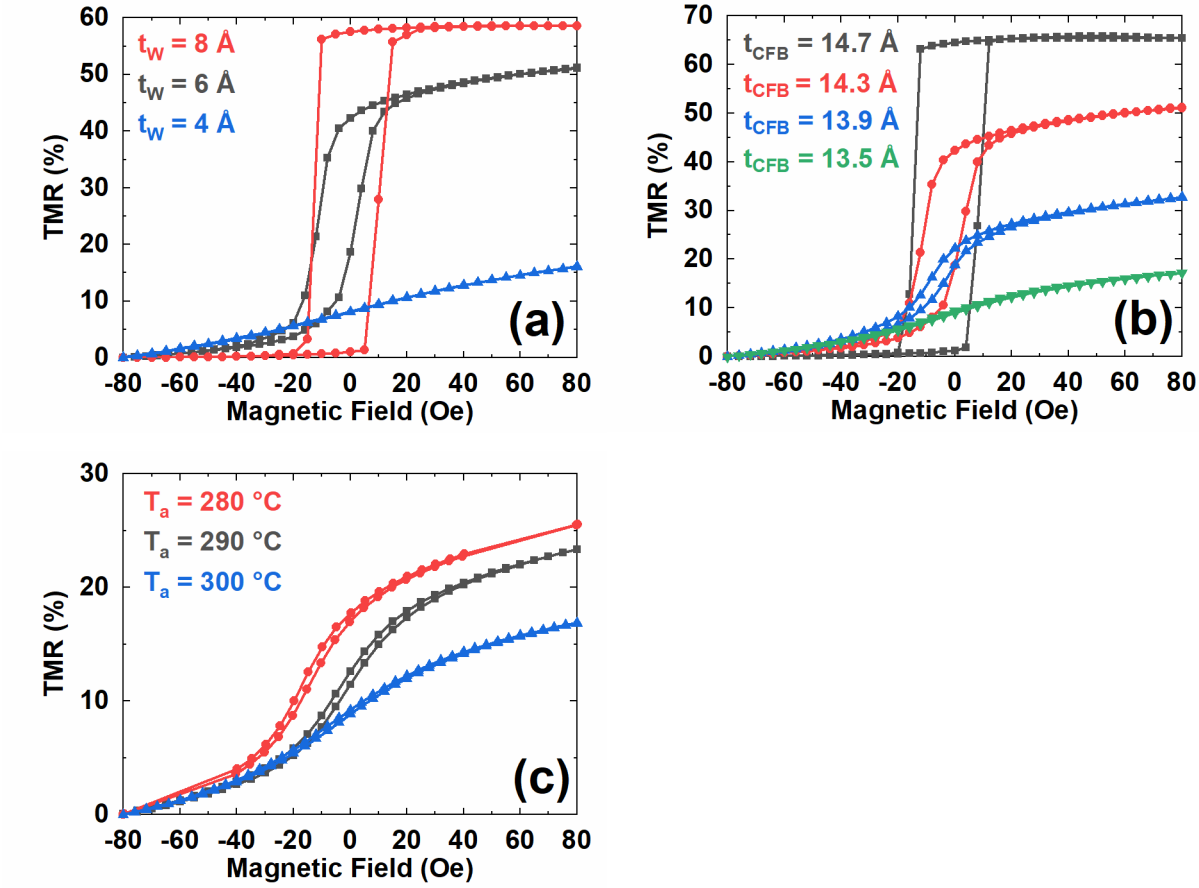


FIG. 1. TMR ratio versus magnetic field (transfer curve) of MTJs incorporating a coupled free layer of $Co_{40}Fe_{40}B_{20}$(9 Å)/W($t_W$)/$Co_{40}Fe_{40}B_{20}$($t_{CFB}$), with (a) different W spacer layer thickness $t_W$, (b) CoFeB layer thickness $t_{CFB}$, and (c) different annealing temperature $T_a$, respectively. The magnetic fields are applied in-plane.

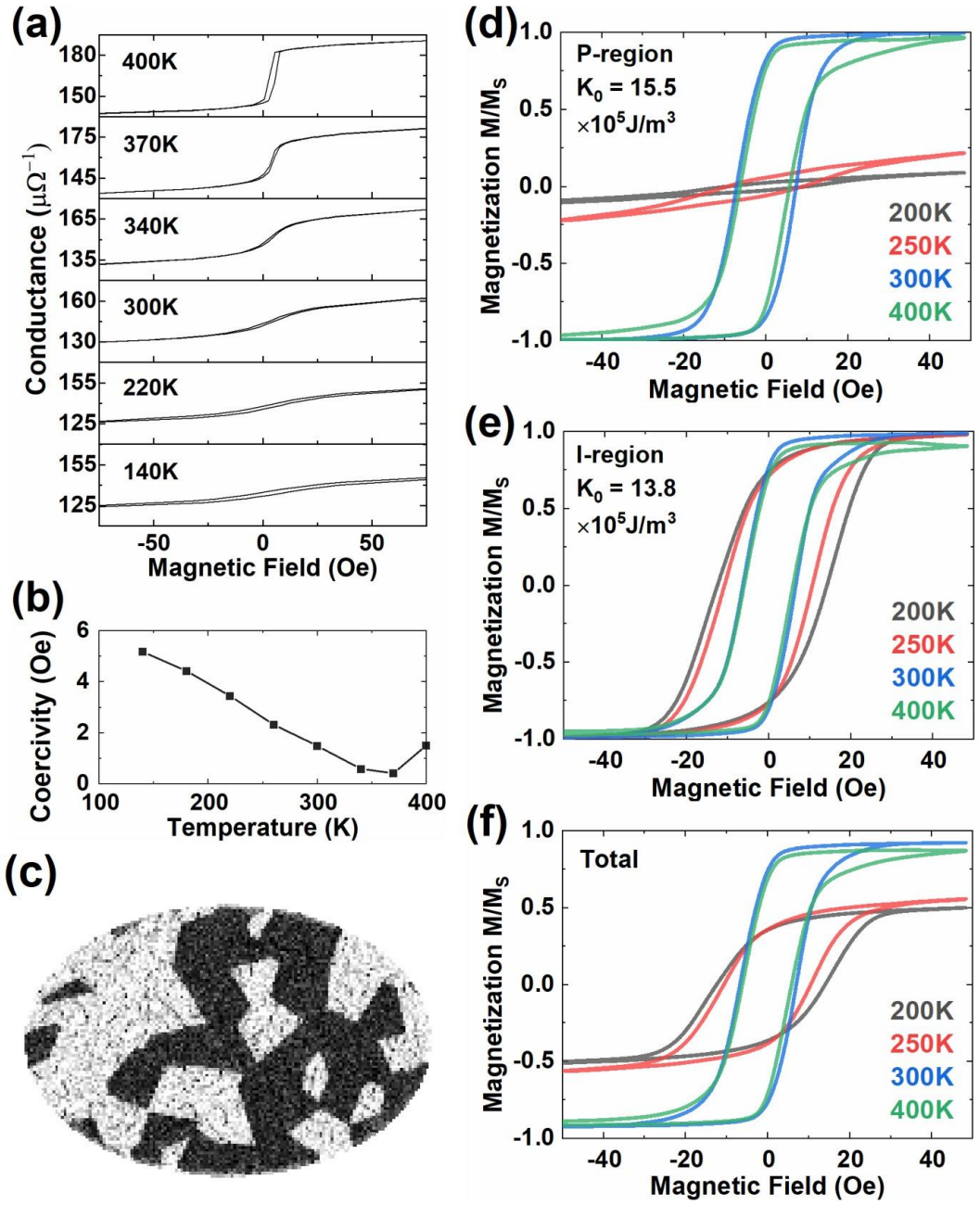


FIG. 2. (a) Magneto-transport measurement of one MTJ ($t_W = 6$ Å, $t_{CFB} = 13.9$ Å, $T_a = 300$ ℃), from 140 K to 400 K. (b) Temperature dependence of magnetic coercivity $H_c$ obtained from (a). (c) Schematic diagram of the micromagnetic simulation of the MTJ free layer, with randomly distributed P-regions and I-regions. Brighter colors indicate stronger magnetizations in the out-of-plane direction, and this magnetization is obtained at 250K, 50 Oe in-plane field. (d) Magnetization transfer curves of the P-region from simulation. (e) Magnetization transfer curves of the I-region from simulation. (f) Total magnetization transfer curves of the MTJ free layer from simulation.

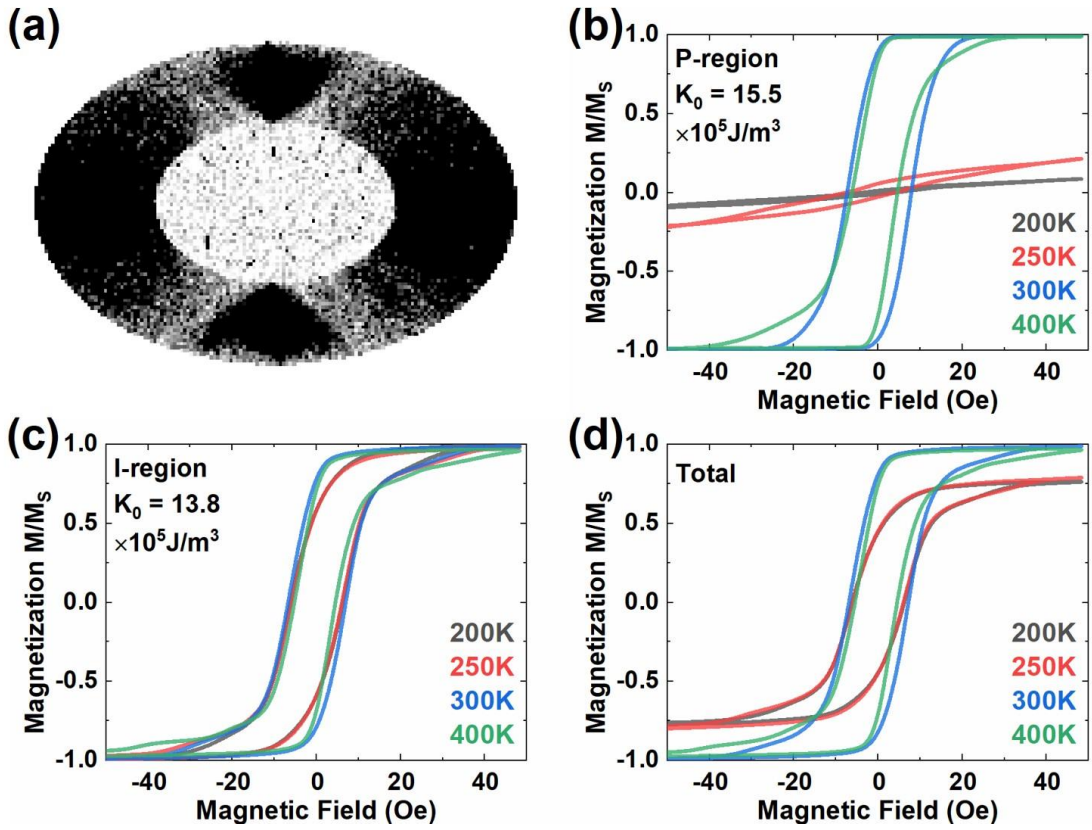


FIG. 3. (a) Schematic diagram of the micromagnetic simulation of the MTJ free layer, with two well-defined P-region and I-region; Brighter colors indicate stronger magnetizations in the out-of-plane direction, and this magnetization is obtained at 200K, 50 Oe in-plane field. (b) Magnetization transfer curve of the P-region from simulation. (c) Magnetization transfer curve of the I-region from simulation. (d) Total magnetization transfer curve of the MTJ free layer from simulation.

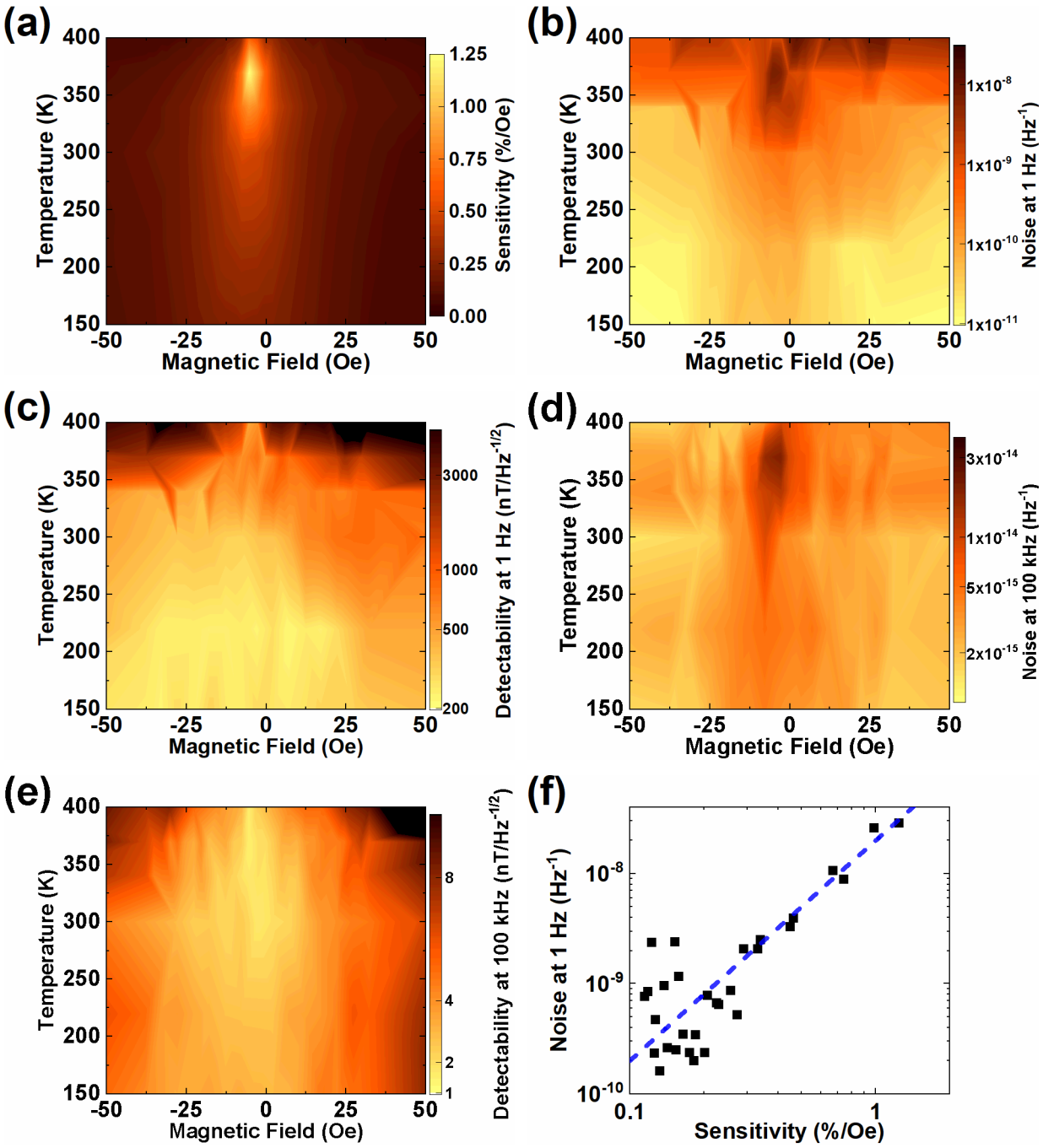


FIG. 4. Magnetic sensing properties of an MTJ with ($t_W$ = 6 Å, $t_{CFB}$ = 13.9 Å, $T_a$ = 300 ℃), measured at different temperatues. (a) Magnetic sensitivity. (b) Normalized noise at 1 Hz. (c) Magnetic field detectability at 1 Hz. (d) Normalized noise at 100 kHz. (e) Magnetic field detectability at 100 kHz. (f) Quadratic scaling relation between the noise and sensitivity at 1 Hz.

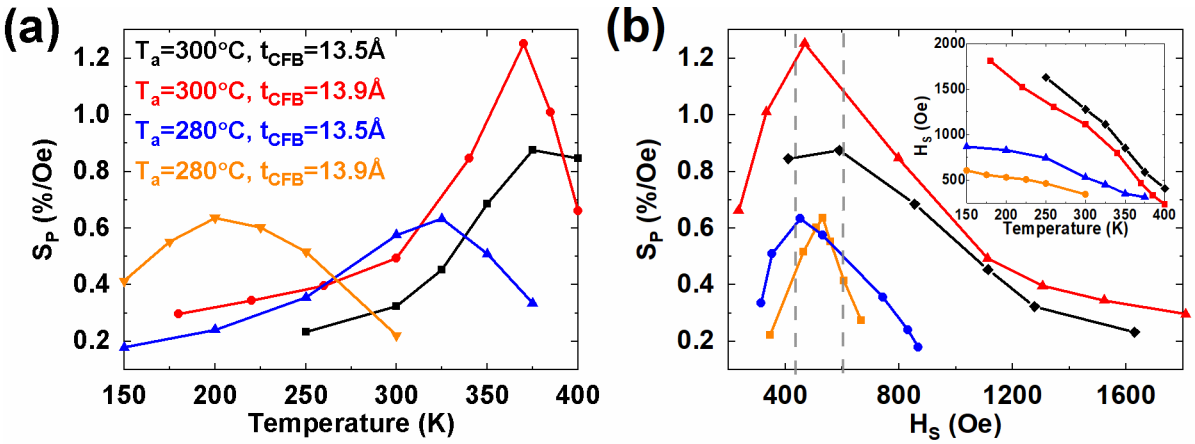


FIG. 5. (a) Peak sensitivity$S_P$ at different temperatures for MTJs with multiple top CoFeB layer thickness $t_{CFB}$ and annealing temperature $T_a$. (b) Relationship between $S_P$ and the in-plane magnetic saturation field $H_S$ for the MTJs in (a). The inset shows $H_S$ versus temperature.

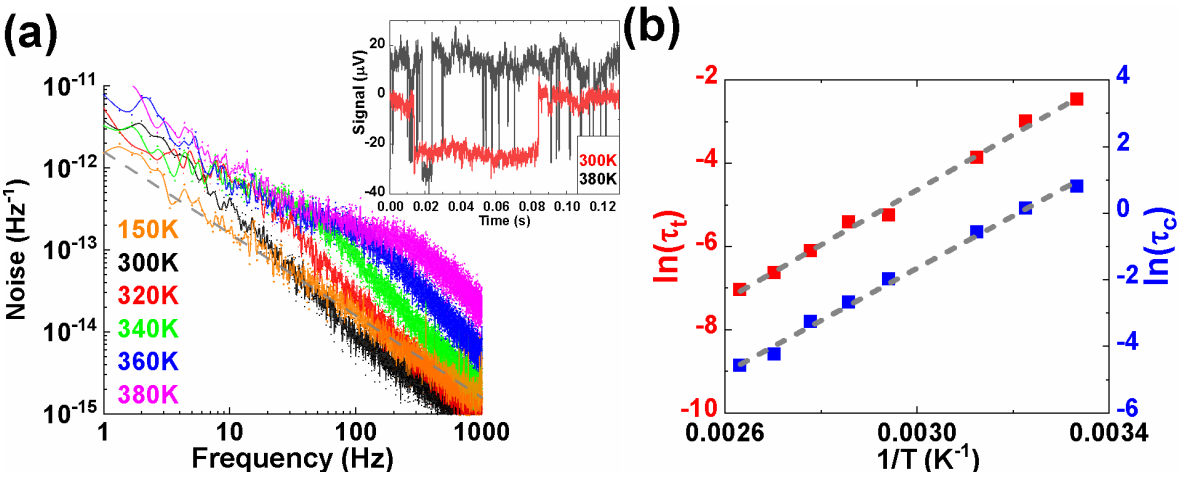


FIG. 6. (a) The Lorentzian spectrum of RTN in a single MTJ at saturation fields, with its corresponding time-domain signal shown in the inset. (b) The relaxation time in two states $\ln(\tau_t)$ , $\ln(\tau_c)$, in proportion to the inverse of temperature.

Table I. Sensitivity and detectability of our MTJs and MTJ sensors with other linearization strategies. Two AHE sensors with compensated magnetic anisotropy are also included. For fair comparison of sensitivity (in unit of V/T), MTJ sensors are assumed to be voltage biased by 100 mV and AHE sensors to be current biased by 1 mA. Also, the magnetic field detectability at 1 Hz $S_T^{1Hz}$ is normalized by the active sensing area $A$. All these results are measured without magnetic flux concentrators.

| Ref. No. | Linearization Strategy | Sensitive Element | Sensitivity (V/T) | $\sqrt{AS_T^{1Hz}}$ $(\mu m\ nT/\sqrt{Hz})$ |
|---|---|---|---|---|
| In our work | Compensated magnetic anisotropy | TMR | 12 | 4298 |
| [36] | Shape anisotropy | TMR | 4.5 | 6753 |
| [37] | Super-paramagnetism | TMR | 10[a] | 3008 |
| [24] | Magnetic vortex state | TMR | 3 | 3125 |
| [38] | Soft pinned free layer | TMR | 30[a] | 7019 |
| [39] | Shape anisotropy | TMR | 1.5[a] | 4048 |
| [11] | Compensated magnetic anisotropy | AHE | 2.5 | 1520[b] |
| [12] | Compensated magnetic anisotropy | AHE | 1.6 | 2520 |

[a] Sensitivity measured from DC transfer curve

[b] Under bias magnetic field of 12 Oe